指向性エネルギー堆積法による Ni625合金の造形プロセスウィンドウ

恵久春佑寿夫，中林拓頌，藤原朋春，Behrang Poorganji

Processing Windows of Ni625 Alloy Fabricated using Direct Energy Deposition[†]

Yusufu EKUBARU, Takuya NAKABAYASHI, Tomoharu FUJIWARA and Behrang POORGANJI

本研究では，ニコン製 Lasermeister レーザー粉末指向性エネルギー堆積（LP-DED）装置を用いた Ni625合金の造形プロセスウィンドウを確立した．プロセスマップは，微細構造と機械的特性の間の相関関係を調べることによって確立された，レーザー出力，スキャン速度，および有効エネルギー密度の関係を示す．全てのサンプルは等軸および柱状デンドライト粒からなる二峰性の微細構造を示し，デンドライトアーム間隔は走査速度の増加に伴い減少した．各サンプルの引張特性はわずかな変動を示し，その値は過去の報告値と同等であった．引張強度および降伏強度は，それぞれ1008 ± 2から 941 ± 9 MPa，682 ± 11から 640 ± 7 MPa の範囲であった．本研究は，様々なパラメータセットにわたる Ni625合金の優れた造形性を実証し，各材料および装置に対して単一の理想的なプロセス条件は存在せず，代わりに同様の結果を得るために複数の「レシピ」を使用できることを示している．

Herein, a process window is developed for Ni625 alloy fabricated using a Nikon Lasermeister laser powder direct energy deposition (LP-DED) unit.

The process map illustrates the relationship between the laser power, scan speed, and effective energy density, established by examining the correlation between the microstructure and mechanical properties. All samples exhibit a bimodal microstructure comprising equiaxed and columnar dendrite grains, and the dendrite arm spacing decreases with increasing scan speed. The tensile behavior of each sample demonstrates minimal variation, and the values are comparable to those reported previously. The ultimate tensile and yield strengths range from 1008 ± 2 to 941 ± 9 and 682 ± 11 to 640 ± 7 MPa, respectively. This study highlights the remarkable manufacturability of Ni625 alloy for additive manufacturing across diverse parameter sets, demonstrating that a single ideal process set does not exist for each material and machine. Instead, multiple “recipes” may be employed to achieve similar outcomes.

Key words 積層造形，レーザー粉末指向性エネルギー堆積法，インコネル625，シミュレーション，微細構造
additive manufacturing, laser powder direct energy deposition, Inconel 625, simulation, microstructure

1 Introduction

Metal additive manufacturing (AM) is an excellent technology for part fabrication, offering distinct advantages over conventional manufacturing methods. With significant cost and lead-time reductions and the capability to develop complex geometrical features [1]–[3], metal AM has rapidly garnered interest from key industries such as aerospace, automotive, military, and biomedical sectors [3]–[5]. Metal AM entails various techniques, including material jetting, sheet lamination, laser powder bed fusion, binder jetting, and direct energy deposition.

Laser powder direct energy deposition (LP-DED) presents unique advantages over other AM processes, including alloy design, repair capabilities, surface modifications, and the synthesis of large-scale components with adequate dimensional accuracy [6]. These capabilities have been increasingly demonstrated and recognized in various fields, particu-

---

[†] This paper uses the following copyrighted work with modifications (*).
Yusufu EKUBARU, Takuya NAKABAYASHI, Tomoharu FUJIWARA, and Behrang POORGANJI, “Processing Windows of Ni625 Alloy Fabricated Using Direct Energy Deposition” Adv. Eng. Mater. 2024, 2400962. (https://doi.org/10.1002/adem.202400962)

* Main content of the modifications
The title, abstract, and author are translated into Japanese, and both English and Japanese are printed.

larly in the aerospace industry [4]. The in-situ alloying of elemental powders offers an effective alternative to the use of pre-alloyed powders, which are cost- and time-intensive to produce using traditional atomization methods. By mixing pure elemental powders of Ni, Cr, Mo, Nb, and Fe, Wang *et al.* [7] demonstrated the high-quality fabrication of Ni625 alloy components using LP-DED and in situ alloying. Wilson *et al.* [8], [9] repaired defective voids in turbine blades, illustrating the effectiveness of LP-DED in repair. These studies highlight the adaptability of DED to a wide range of defective parts, as well as its capabilities in repair and maintenance. Balla *et al.* [10] applied a tantalum coating onto titanium using LP-DED, a notable achievement considering the extremely high melting point (>3000°C) of Ta, which poses challenges for traditional melt-cast methods. Ta-coated Ti exhibits favorable interactions with bone cells, indicating promising biocompatibility. Gradl *et al.* [1], [2], [11] utilized LP-DED to manufacture a large-scale rocket nozzle for aerospace applications. The growing recognition of LP-DED is reflected in the significant increase in the number of patents and scientific publications dedicated to this technology, highlighting its importance in academia and industry [5], [12].

Furthermore, the anticipation of an expanding market for AM has spurred intense competition among AM machine manufacturers, resulting in the development of various AM systems [4]. In this context, Nikon Advanced Manufacturing Business Unit in Japan developed an LP-DED system named Lasermeister. Extensive empirical testing has been conducted on this machine with common AM materials, including Fe-, Ni-, and Ti-based alloys. Herein, we present our latest research findings, particularly focusing on the Ni625 alloy, also referred to as Alloy 625 or Inconel 625.

The Ni625 alloy has been utilized in various industries, including petrochemical, aerospace, chemical, marine, and nuclear sectors, due to its excellent strength and high corrosion and fatigue resistance [12], [13]. Moreover, its remarkable weldability has attracted considerable attention in AM, where it has been successfully produced using various process parameters in LP-DED, including laser power (P) (220–1500 W) and scan speed (V) (8.3–33.3 mm/s), with the corresponding effective energy density (E_D) ranging from 14 to 66 J/mm^2 [7], [13]–[20].

The solidification microstructure of AM-produced Ni625 alloy is complex, featuring fine dendrites, micro-segregated elements, and various solidification phases [21]. The nickel-based superalloy, primarily strengthened by the solid hardening effects of refractory elements including niobium and molybdenum within a nickel-chromium matrix exhibits a face-centered cubic (FCC) structure [14]. These alloys are sensitive to the precipitation of strengthening intermetallic phases, including stable ordered FCC ($L1_2$) γ'-Ni_3Al; metastable body-centered tetragonal γ''-Ni_3Nb; stable orthorhombic d-Ni_3Nb; carbides (MC, M_6C); and intergranular brittle Laves phases ((Nb, Mo)$(NiCrFe)_2$) in the interdendritic region [1], [12]–[14]. The formation of these phases, particularly the Laves phases, consumes significant amounts of Nb and Mo, thereby reducing their content in the matrix, which diminishes solid solution and precipitation strengthening effects [19]. Further, the Laves phase induces crack nucleation and propagation, significantly deteriorating creep rupture properties and ductility [19]. Consequently, manufacturing components with reduced elemental segregation and fewer Laves phases has become critical.

The mechanical properties of materials are primarily influenced by factors such as porosity, grain size, the behavior of precipitates, and dendrite spacing [25]. Generally, the mechanical properties can be improved by reducing their size, which essentially means creating a finer microstructure. Reducing porosity can enhance the material's strength and durability as fewer pores mean less space for cracks to initiate. Smaller grain sizes often lead to increased hardness and strength due to the Hall-Petch relationship. Controlling the behavior of precipitates, such as reducing their size, can increase the material's strength as smaller precipitates more effectively hinder dislocation movement [25], [26]. Lastly, smaller dendrite spacing can contribute to a more homogeneous microstructure, reducing segregation and enhancing various mechanical properties [25], [26]. One fundamental approach to achieving a finer microstructure is to increase the cooling rate, and it can be accomplished by using a smaller P, a higher V, or a combination of both [27].

Based on this background, this study aimed to a) develop the process windows for Ni625 alloy using the Lasermeister system and b) establish a process window that expresses the relationship between P, V, and E_D based on a series of simulations and experiments focusing on microstructural properties and mechanical performance.

This research demonstrated for the first time that using lower P values and smaller hatch spacings can significantly enhance the strength of Ni625 alloys by promoting substantial microstructure miniaturization. Additionally, DED process "recipes" for Ni625 in the lower P region were developed. These results are expected to significantly contribute to the DED fabrication of components such as precise, large, thin-walled structures that are vulnerable to thermal deformation, as well as the automation of gas turbine blade repairs, among other applications.

Table 1 Chemical composition (wt%) of Ni625 alloy

Powder	Ni	Cr	Mo	Nb + Ta	Fe	Al	Ti	C	Mn
Inconel625	Bal.	20–23	8–10	3.15–4.15	≤ 5	≤ 0.4	≤ 0.4	≤ 0.03	≤ 0.01

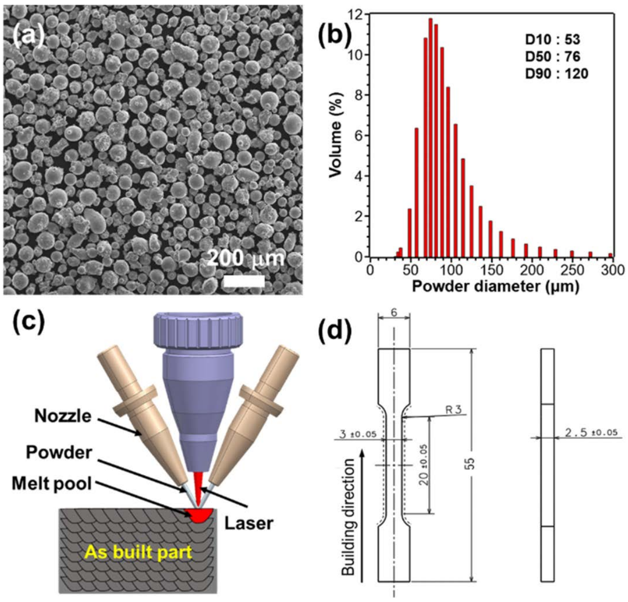

Fig. 1 (a) Morphology and (b) powder size distribution of the Ni625 alloy powders used in LP-DED (c) Schematic of LP-DED and (d) dimensions of the tensile test sample

2 Experimental Section

2.1. Ni625 Alloy Fabrication

Ni625 alloy powders were procured from Carpenter Additive Inc.; and their compositions and morphologies are summarized in Table 1 and Fig. 1, respectively. An LP-DED unit (Lasermeister 100A) with a 915 nm 200 W laser diode module and a beam diameter (d) of 0.5 mm was utilized to fabricate the Ni625 alloy samples (Fig. 1 (c)). Two samples, namely, a 10 mm × 10 mm × 10 mm cube and a 10 mm × 10 mm × 55 mm rectangle, were fabricated along the x-, y-, and z-axes on a SUS304 substrate via the XY scanning strategy. Cubic samples were used for microstructural analysis, whereas rectangular samples were employed for tensile property testing (Fig. 1 (d)) [7], [20]. The parameter values used for the experiment are listed in Table 3, where the laser hatch spacing was maintained at 0.2 mm.

2.2. Microstructure Characterization and Mechanical Properties

Samples were cut from the substrate via electrical discharge machining to analyze their microstructures and mechanical properties. The YZ cross sections were first mechanically polished using emery paper up to a 4000 grade and subsequently chemically polished with colloidal silica to achieve mirror-polished sections for microstructural examination.

Optical microscopy (VHX8000, KEYENCE, Osaka, Japan) and scanning electron microscopy (SEM; SU1500, Hitachi High-Tech Corporation, Tokyo, Japan) were conducted to examine the microstructures. The bulk samples fabricated by the LP-DED Lasermeister were characterized via X-ray diffraction (XRD; RINT2500,Rigaku Corporation, Tokyo, Japan) with Cu-Ka radiation at room temperature (RT). Crystallographic texture and elemental segregation were investigated using electron backscattered diffraction (EBSD) and energy-dispersive X-ray spectroscopy (EDS), respectively, with a scanning electron microscope (JSM-7900F,JEOL Ltd., Tokyo, Japan). A tensile test (TGI-50KN, MinebeaMitsumi Inc., Nagano, Japan) was conducted at RT, where the loading axis was parallel to the build direction (BD). The test was conducted thrice for each sample, and the results were averaged.

2.3. Simulations

The formation mechanism of the microstructure induced by LP-DED was explored through simulations focusing on thermal behavior and solidification characteristics. The thermal behavior calculations provided insights into the temperature distribution and the shape and size of the melt pool (MP). Conversely, analyzing the solidification characteristics aided in understanding the development of grains, which could manifest as either equiaxed dendrites (ED) or columnar dendrites (CD).

These simulations were performed using the commercial software FLOW-3D v12.0 for a region measuring 10 mm × 7 mm × 3 mm in the X, Y, and Z directions. The region was discretized into a structural Eulerian mesh with a size of 0.025 mm.

2.3.1. Heat Source Model

$$q_{in} = \left(\frac{P_0}{\pi r_b^2}\right)\exp\left\{-\left(\frac{r}{r_b}\right)^2\right\} - h_c\left(T - T_0\right) \tag{1}$$

where P_0 is the laser power (100/120/160 W), r is the distance from the beam center, r is the laser radius (0.25 mm), r_b is the effective laser radius (0.1 mm), h_c is the heat transfer coefficient (9.5 W/m^2 K) [28], T is the temperature, and T_0 is the ambient temperature (298 K).

2.3.2. Powder Model

We employed the Lagrangian particle tracking method to model the powder particles. Particles entering the melt pool transformed into liquid cells upon surpassing the melting point. The amount of powder injected was calculated from the predetermined powder utilization efficiency. The powder was injected at a constant velocity from the vertical direction of the melt pool to ensure the melting of all particles.

2.3.3. MP Flow Governing Equations

The governing equations, which include mass, momentum, and energy conservation, are expressed in (2), (3), and (4), respectively.

$$\frac{\partial \rho}{\partial t}+\nabla \cdot \rho v=R_{SOR} \tag{2}$$

$$\frac{\partial \boldsymbol{v}}{\partial t}+(\boldsymbol{v}\cdot\nabla)v=-\frac{1}{\rho}\nabla p+\frac{\mu}{\rho}\nabla^2 v+g-\frac{R_{SOR}}{\rho}(\boldsymbol{v}-\boldsymbol{v}_p) \tag{3}$$

$$\frac{\partial(\rho I)}{\partial t}+\nabla\cdot(\rho I\boldsymbol{v})=-p\nabla\cdot v+k\nabla^2 T+I_{SOR} \tag{4}$$

$$I=C_v T+(1-f_s)L \tag{5}$$

where ρ is density, t is time, v is flow velocity, R_{SOR} is the amount of mass source due to powder particles, p is pressure, m is viscosity, v_{p} is particle velocity, Cv is specific heat, fs is the solidus rate, I_{SOR} is the discharge of energy, and L is latent heat. The thermophysical parameters were calculated using the thermodynamic database of JmatPro (Sente Software) considering their temperature dependencies (Table 2).

2.3.4. Solidification Parameter

The temperature gradient G and solidification velocity R represent spatial temperature variations and are expressed as:

$$\varepsilon=\left|\frac{T_s-T_L}{t_s-t_L}\right| \tag{6}$$

$$G=\nabla T \tag{7}$$

$$R=\frac{\varepsilon}{|\boldsymbol{G}|} \tag{8}$$

where e is the cooling rate, T_{s} is the solidus line temperature (1398 K), T_{L} is the liquidus line temperature (1613 K), t_{S} is the time below the solidus line temperature, t_{L} is the time below the liquidus line temperature, and ∇ is the differential operator.

3 Results

3.1. Simulated Data

The aspect ratio (D/W), indicating the depth (D) to width (W) ratio of the MP, was assessed in both the experimental and simulated scenarios to verify the simulation model. Fig. 2 displays the results of the single-track experiments and simulations at V values of 5 and 10 mm/s, with constant P and powder feeding rate (Q) values of 120 W and 3 g/min, respectively. The experimental dimensions of the MP were measured from the optical images, whereas the simulated sizes of the MP were determined by identifying a black solidus line on the temperature contour map. The aspect ratios decreased with increasing V, and the experimental aspect ratios were slightly higher than the simulated ones, with differences of < 10%. It is considered that one possible reason for this difference is the thermal boundary conditions of the

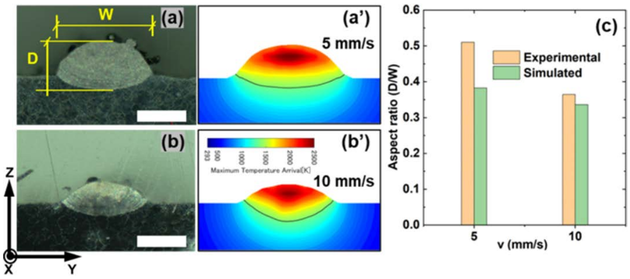

Fig. 2 Comparison of the experimental and simulated MP: (a) and (b) experimental optical images, (a') and (b') simulated temperature contours, and (c) aspect ratio
Scale bars: 200 mm

Table 2 Thermophysical properties of Ni625 calculated using JmatPro

Temperature intervals T (K)	Thermal conductivity k (W/(m K))	Specific heat Cv (J/(kg K))	Density r (kg/m^3)	Viscosity m (kg/(m s))	Surface tension s (N/m)	Latent heat of fusion L (kJ/kg)
298	10.8	406	8474	-	-	210
600	15.9	456	8373	-	-	
900	20.9	504	8253	-	-	
1200	25.8	559	8117	-	-	
1500	30.1	713	7931	1.39×10^{-2}	1.84	
1800	31.4	737	7499	0.62×10^{-2}	1.74	
2100	35.8	745	7235	0.38×10^{-2}	1.62	
2400	40.2	748	6952	0.26×10^{-2}	1.52	

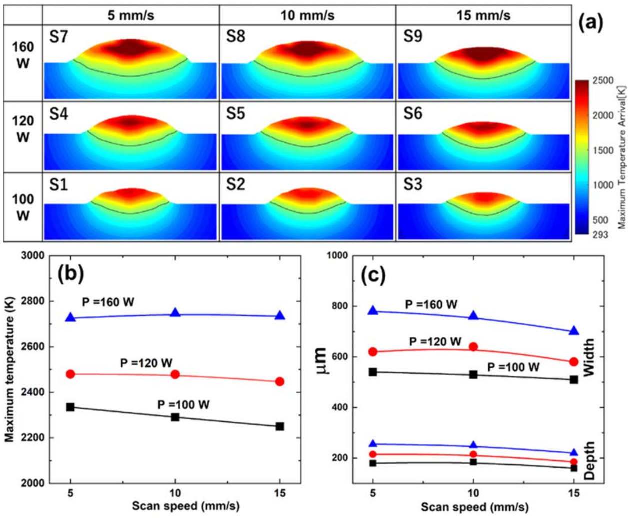

Fig. 3 Simulated MP of (a) temperature contour plot, (b) maximum temperature, and (c) dimensions at varying process parameters

substrate in the simulation. Hence, this model was employed for additional simulations to generate a process map for the Ni625 alloy.

Various conditions were simulated to assess fabrication feasibility using these process parameters. Fig. 3 illustrates the simulated temperature contour plots and the maximum temperature of the MPs under nine different conditions, accompanied by their respective sizes. As shown in Figs. 3(b) and 3(c), with an increase in P from 100 to 160 W (while V is constant at 5 mm/s), the maximum temperature increases from 2335 to 2725 K, and the width of the MPs increases from 540 to 780 mm; by contrast, increasing V when P is constant causes both the maximum temperature and the width and depth of the MPs to remain almost constant. The highest temperatures and dimensions of the MPs indicated a significant dependence on P but less dependence on V. Consequently, MPs were formed under all conditions, and the maximum temperature exceeded the melting point of the Ni625 alloy at 1623 K [29], which allowed us to proceed with the experiments.

3.2. Microstructural Analysis

The fabricated state, porosity, and cracks of the samples produced under the nine simulated conditions were investigated via cross-sectional image analysis using an optical microscope. All samples, except S7, were successfully manufactured, as shown in Fig. 4(a); however, S7 could not be completed because the powder adhered to the nozzle owing to the highest energy density input. The optical density shown in Fig. 4(b) was measured from optical images of the polished surfaces of the samples. Five images were taken from different locations on the polished surface of each sample at 200X magnification. The optical density of these images was then measured using ImageJ software, and the average was calculated. As shown in Fig. 4(b), most samples, excluding S2 and S3, exhibited a dense structure without any visible cracks; this resulted in a satisfactory industrial density of over 99.5% [3], [30], [31]. However, samples S2 and S3 showed noticeably lower density values with irregularly shaped pores caused by the lack of fusion owing to the lower energy density input. It can be generally observed that densification increases with increasing P and decreases with increasing V. This behavior is more significant in samples S1 to S3 at 100 W, while it is less pronounced in samples S4 to S9 at 120 W and 160 W. This suggests that at lower P settings, the impact of V on densification is more pronounced, whereas at higher P settings, the effect of V becomes less significant. Consequently, optimizing P and V parameters is crucial for achieving desired densification levels in different samples.

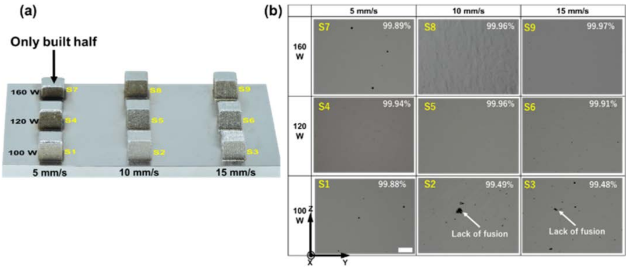

Fig. 4 (a) Appearance of the LP-DED fabricated samples and (b) optical density

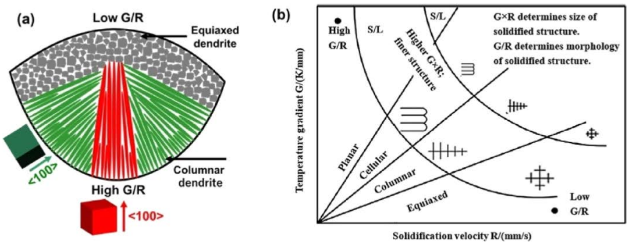

Fig. 5 (a) Schematic of the MP microstructure and (b) columnar-equiaxed transition criteria, adapted from [27] with permission [27], [32], [33]

The microstructure of AM materials can be explained by the MP microstructure using Hunt's columnar-equiaxed transition criteria [27], [32], [33]. As shown in Fig. 5(a), MPs typically exhibit a bimodal microstructure comprising two types of grains: ED at the top with no preferential crystallographic orientation and CD at the bottom that show a preference for growing from the bottom part to the center along the direction of the thermal gradient [21], [33]–[35]. This is attributed to the higher G/R ratio at the bottom part of the MP and the lower G/R ratio at the top, as illustrated in Fig. 5(b), where

G/R is the grain morphology factor determining either ED or CD, and G × R is the cooling rate that determines the size of the grain. Typically, the extremely high G and G × R values in the AM process foster directional solidification, and enhance the textures of the microstructures of alloys [36], [37].

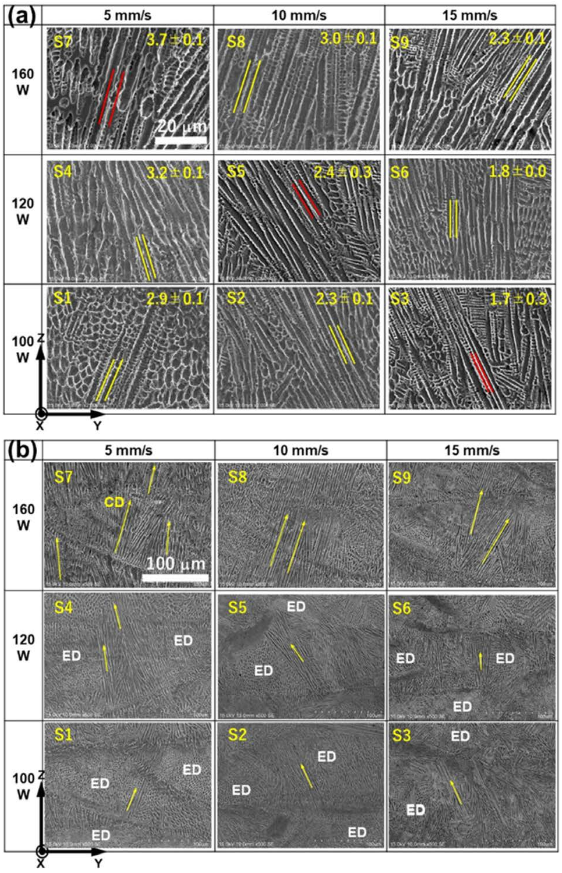

Fig. 6 SEM images of the YZ plane of the samples with (a) higher magnitudes containing PDAS and (b) lower magnitudes containing CD and ED regions

The dendrite microstructural features, including the PDAS size and shape of the grains of the samples, were characterized by observing the SEM images of the aqua regia-etched YZ cross-section. PDAS is one of the factors in influencing mechanical properties and it was known that smaller PDAS increases various mechanical properties [25], [26]. As shown in Fig. 6(a), among the samples, S7 yielded the highest PDAS with a value of 3.7 ± 0.1 mm, while S3 yielded the lowest PDAS with a value of 1.7 ± 0.3 mm; consequently, the PDAS increased as the P increased and V decreased. In contrast, as shown in Fig. 6(b), all samples exhibited a bimodal grain microstructure consisting of CD and ED regions. Samples S7 to S9, fabricated with the highest P of 160 W, exhibited a predominance of CD, while samples S1 to S3, fabricated with the lowest P of 100 W, displayed an almost exclusive ED presence, and resulted in a trend that shifted from an ED-dominant to CD-dominant microstructure with increasing P and decreasing V, respectively; namely, high P values increased the dendrite structure, which is consistent with other research [14].

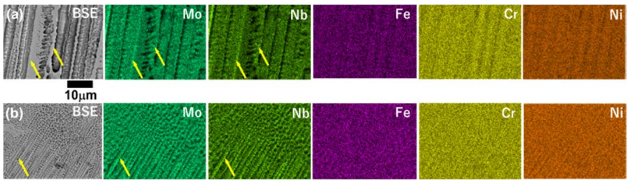

Fig. 7 EDS maps of samples of (a) S7 and (b) S3

The elemental microsegregation of the samples was analyzed using EDS mapping. Figs. 7(a) and 7(b) illustrate the distributions of the main elements (Ni, Cr, Fe, Nb, and Mo) in samples S7 (with the highest energy density) and S3, respectively. The Mo and Nb contents in the interdendritic regions were higher than those in the dendritic regions, as indicated by the yellow arrow. Both samples exhibited significant Mo and Nb segregation with no clear differences in their segregation behaviors. Based on the obtained results and previous reports, it can be concluded that the observed phase corresponds to the Laves phase [7], [16], [19]

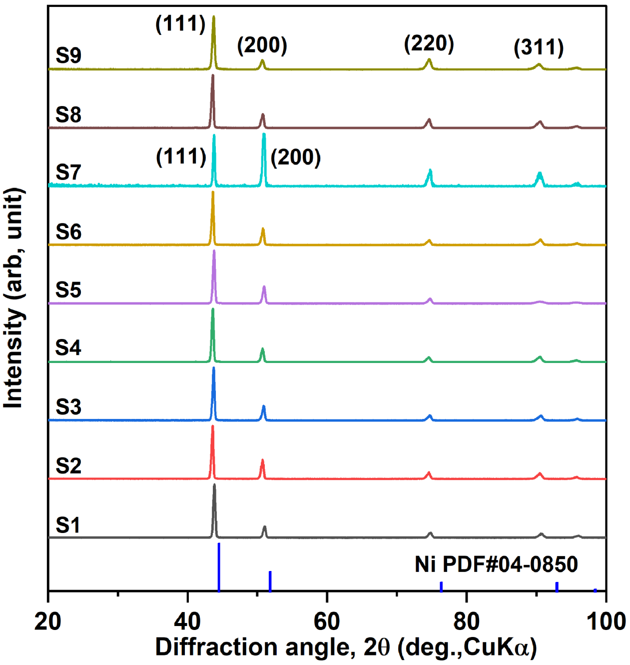

Fig. 8 XRD patterns of the LP-DED fabricated samples

XRD analysis was conducted on the polished YZ cross-section of the samples to confirm the phase states. As shown in Fig. 8, all the samples exhibited peaks corresponding to the reference Ni (PDF #04-0850) in the XRD analysis. Interestingly, in sample S7, the relative intensities of the (111) and (200) peaks were similar, even though (111) has the highest-intensity peak, indicating that (100) tends to be oriented in the BD (z-direction), which is in agreement with other studies [3], [7], [38], [39]. However, all samples exhibited a minor peak shift to a lower diffraction angle compared with Ni (PDF #04-0850), implying the presence of residual stress in the samples [3], [38].

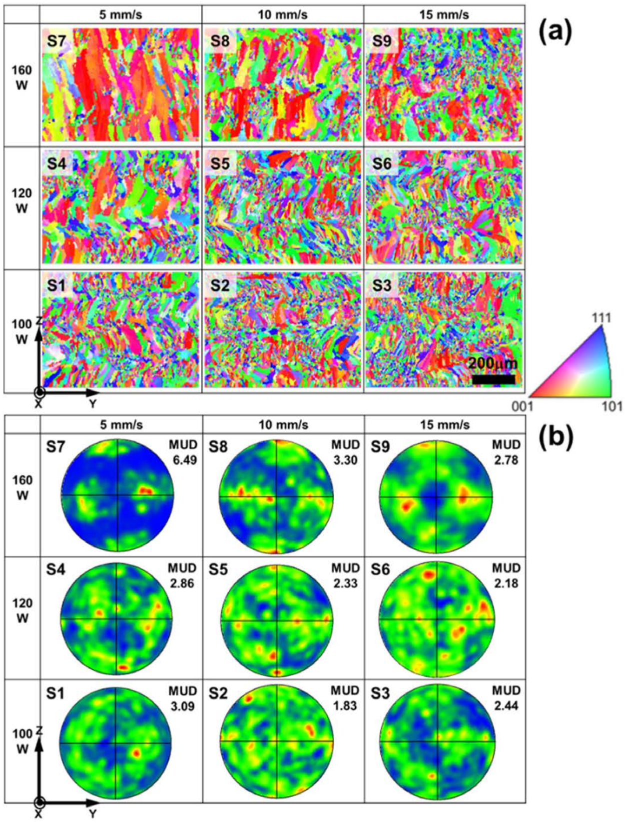

Fig. 9 EBSD (a) inverse pole figure maps and (b) the corresponding {001} pole figures with multiples of uniform distribution (MUD) values of the YZ plane

One of the key features of AM that influences the mechanical properties is the crystallographic texture [36], which was investigated using EBSD. As shown in Fig. 9 (a), by increasing P and decreasing V, directional grain growth occurs along the *z*-direction with a {100} crystallographic orientation, which is an easy growth direction for the FCC crystal structure [3], [36], which was observed in the samples. The values of the texture strength measure, MUD, increased as P increased and V decreased; however, apart from sample S7, no distinguishable crystallographic textures were observed for the samples, and S7 exhibited the highest texture with most grains aligned in the {100} crystallographic orientation; this finding is consistent with the XRD results shown in Fig. 8.

3.3. Tensile Properties

A tensile test was performed at RT, and the results showed trends corresponding to the features of the microstructure. As shown in the optical images in Fig. 4, the porosity increased with V in the sample fabricated at the lowest P of 100 W, whereas the elongation (El) of these samples decreased, as shown in Fig. 10(a). However, with an increase in V, the minor decreases in the PDAS and grain size shown in Figs. 6 and 9 led to a minor monotonic increase in the ultimate tensile strength (UTS) for the samples produced at P = 120 W and 160 W. Consequently, the tensile properties exhibited negligible variations because fewer changes were observed in the microstructure.

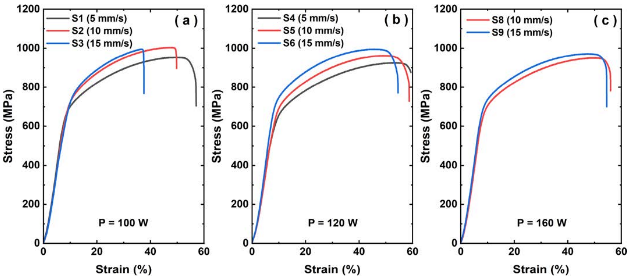

Fig. 10 Tensile stress-strain curves of the samples

3.4. Process Window

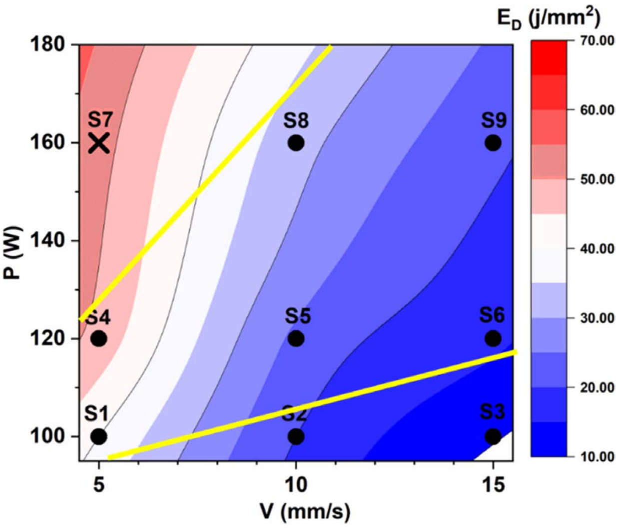

Fig. 11 P–V process map with E_D contour

A process map illustrating the relationship between P, V, E_D and the feasibility of sample fabrication was established based on the experimental data obtained in this study. Fig. 11 illustrates that the pink region represents high E_D, while the blue region represents low E_D. Additionally, samples S2 and S3, located in the low E_D area, exhibited higher porosity owing to insufficient fusion. Conversely, sample S7, situated in the high E_D area, was not fully produced because of powder adhesion in the nozzle. Consequently, the approximate optimal region is indicated by a yellow line.

4 Discussion

4.1. Pore Formation and Mechanical Property Impact

Pores are one of the major defects that significantly affect the mechanical properties of parts; which can primarily occur owing to both high- or low-energy input, as well as the insufficient overlap of laser tracks [40].

High-energy input during the melting process can result in the formation of an unstable MP at extremely high temperatures and severe Marangoni convection, which in turn leads to the generation of spherical pores either by trapping the protective gas (Ar) or metallic vapor [3], [40]. As shown in Fig. 4(b), samples S7 and S1 fabricated with a higher energy density showed spherical pores with a maximum diameter of 40 mm. These pores were primarily formed owing to the trapping of Ar gas and were unlikely attributed to metallic vapor because of the high melting points of all the main elements of the Ni625 alloy. It is known that spherical pores with diameters < 130 μm have negligible detrimental effects on the mechanical properties of the material [3]. Moreover, as illustrated in Fig. 10(a), sample S1 displayed satisfactory tensile properties, despite the presence of spherical pores.

Low-energy input cannot completely melt the metallic powder in the previously deposited layer, thus leading to irregularly shaped lack of fusion pores, as shown in Fig. 4(b). Samples S2 and S3 produced with lower energy input contained irregularly shaped pores with sizes over 100 mm; these samples exhibited lower elongation tensile properties, as shown in Fig. 10(a).

Insufficient overlap among laser tracks can also cause a lack of fusion pores, which may be attributed to a large hatch distance and/or layer thickness [40]. However, in this study, the primary cause of the lack of fusion pores was identified as low-energy input, predominantly due to low P.

4.2. Effects of P and V on Grain Size and Morphology

P and V are the primary process parameters used to adjust the energy density to tailor the microstructure, and they significantly affect the MP solidification process parameters G and R [27], [32], [33]. Therefore, a comprehensive understanding of G and R is crucial for predicting or explaining the microstructural features observed in experimental samples, and simulations are an effective tool for their calculation [27], [41], [42].

As shown in the solidification map in Fig. 5(b), G × R is the cooling rate that determines the size of the grain, whereas (G/R) is the morphology factor that determines the shapes of the grains. In this study, a maximum cooling rate of 3.5×10^4 K/s was achieved for sample S3, which is close to the intrinsic cooling rate of LP-DED, which ranges from 10^3 to 10^4 K/s [21].

At increasing P and decreasing V values, the PDAS increased while the grain shapes shifted from being predominantly ED-dominant to CD-dominant, as shown in Fig. 6(b). It is believed that these behaviors can be attributed to the changes in G × R and G/R, as illustrated in Fig. 12.

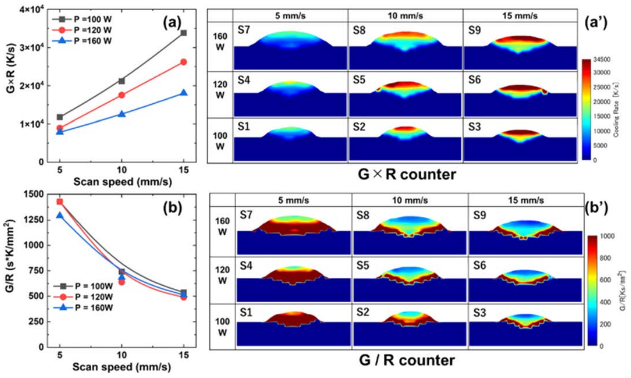

Fig. 12 Simulated (a) average G × R and (a') G × R contours, and (b) average G/R and (b') G/R contours

As shown in Fig. 12(a), the impact of P on G × R is minor at low V values but becomes significant at high V. Therefore, the G × R values of the samples are almost the same at V = 5 mm/s, and the PDASs of these samples do not change significantly, as shown in Fig. 6(a). Conversely, G × R increased as a function of V as also proven by other researchers [27], [41], [42], and the highest and lowest G × R values were obtained for S3 and S7, respectively; accordingly, S3 and S7 respectively exhibited the lowest and highest PDAS values equal to 1.7 ± 0.3 mm and 3.7 ± 0.1 mm, as shown Fig. 6(a).

As shown in Fig. 12(b), G/R is less affected by P but is significantly affected by V; additionally, G/R decreases as V increases, thus suggesting that CD increases with decreasing V. Correspondingly, the directional grain growth along the *z*-direction with the {100} crystallographic orientation is most significant in the samples with the lowest V of 5 mm/s, as shown in Fig. 9.

As shown in Figs. 12(a') and 12(b'), higher G/R and lower G × R values are observed at the bottom of the MP; in contrast, lower G/R and higher G × R were obtained at the top of the MP [27], [41], [42] and these behaviors are most significant at low V, thus indicating that the morphology of the microstructure is prone to CD. Correspondingly, the texture strength measure MUDs were higher in fabricated samples with the lowest V, as shown in Fig. 9.

4.3. Verification of Tensile Properties

Although there were no dramatic differences in the tensile behavior of each sample in this study, the results were still comparable to the tensile results from other existing studies. As illustrated in Fig. 13 and as listed in Table 3, the UTS and yield strengths (YS) of samples exhibited minor changes, with UTS changing from 1008 ± 2 to 941 ± 9 MPa and YS changing from 682 ± 11 to 640 ± 7 MPa. However, in the samples fabricated with the lowest P of 100 W, the elongation noticeably decreased as V increased owing to the higher porosity caused by the lack of fusion, as shown in Fig. 4. Conversely, according to the reference data in Table 3, it is known that the Ni625 alloy can be fabricated using a broad range of process parameters (for example, P may change from 220 to 1500 W and V from 8.3 to 33.3 mm/s) yielding higher tensile properties than casting.

In addition, based on the literature data listed in Table 3, the UTS decreases at increasing P. A higher P not only increases the evaporation [21] of Al, Cr, Fe, and Co in the Ni625 alloy by increasing the MP temperature, but also accelerates precipitation growth owing to a lower cooling rate, thus leading to a degradation of mechanical properties. Therefore, using P values as small as possible is advantageous for the microstructure and mechanical properties of the material and machine maintenance. In this study, tensile properties similar to those reported in other research studies [7],[13],[14],[18] were obtained by using a lower P combination with a small hatch space, as shown in Fig. 13. A small hatch space increases remelting, which reduces the lack of fusion [43] and increases the ED grains [3].

This study is believed to be the first report on the optimization of the strength and ductility of Ni625 alloys using a relatively low P value, thus demonstrating that high-performance Ni625 alloys can also be fabricated with lower P.

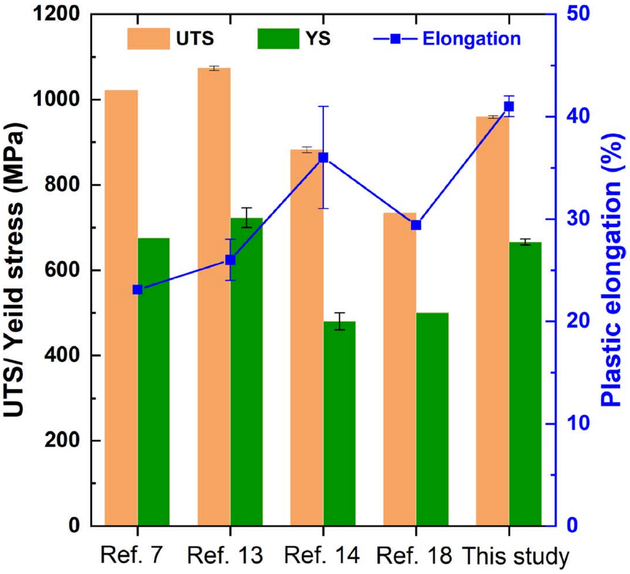

Fig. 13 Comparison of tensile properties in this study with those obtained in other research studies

5 Conclusion

Extensive empirical testing on the Lasermeister was performed with common AM materials, including Fe-, Ni-, and Ti-based alloys. Herein, to develop process maps for the Ni625 alloy specific to this machine, the processability, microstructure, and mechanical properties of the alloy were experimentally and numerically investigated under various

Table 3 Comparison of process parameters and tensile properties in this study with those obtained in references

Label	*P* (W)	*V* (mm/s)	*Q* (g/min)	*d* (mm)	$E_D = P/(Vd)$ (J/mm^2)	UTS (MPa)	YS (MPa)	El (%)
S1	100	5.0	2.0	0.5	40.0	951 ± 7	655 ± 15	42 ± 2
S2	100	10.0	4.0	0.5	20.0	1008 ± 2	682 ± 11	36 ± 1
S3	100	15.0	4.0	0.5	13.3	1005 ± 7	674 ± 13	28 ± 4
S4	120	5.0	2.0	0.5	48.0	941 ± 9	640 ± 7	42 ± 2
S5	120	10.0	4.0	0.5	24.0	959 ± 3	666 ± 7	41 ± 1
S6	120	15.0	4.0	0.5	16.0	989 ± 4	669 ± 12	37 ± 1
S7	160	5.0	2.0	0.5	64.0	-	-	-
S8	160	10.0	4.0	0.5	32.0	944 ± 4	670 ± 10	42 ± 1
S9	160	15.0	4.0	0.5	21.3	960 ± 6	672 ± 9	40 ± 1
[7]	220	8.3	2.3	0.4	66.0	1020.9	675.8	23.1
[14]	330	33.3	7.0	0.4	14.1	1073 ± 5	723 ± 23	26 ± 2
[15]	500	12.5	2.5	1.2	33.3	882 ± 7	480 ± 20	36 ± 5
[19]	1500	15.0	7.5	5	20.0	733.7	500.4	29.4
[29]	Casting	485.0	275.0	25.0				

fabrication parameters. Key findings include:

1. A simulation model was established to predict the MP thermal history, including the dimensions and G and R rates.
2. The dimensions and highest temperatures of the MP were considerably affected by P but less affected by V, leading to high P values and increased size and maximum temperature of the MP.
3. Fully dense Ni625 alloy parts (> 99.5%) were fabricated under conditions where P was > 100 W and V was in the range of 5–15 mm/s.
4. As P increased and V decreased, a corresponding increase in the dendritic structure and texture was observed. Notably, the sample synthesized with the highest P value of 160 W and lowest V value of 5 mm/s exhibited the most pronounced dendritic structure and texture.
5. A positive correlation was observed between the microstructure and tensile properties with lower elongations for finer microstructures. In particular, sample S3, which had the finest microstructure and highest porosity, exhibited the lowest elongation.
6. P ranged from 100 to 160 W, V varied between 5 and 15 mm/s, and a corresponding process map for E_D was established.
7. The samples showed tensile strength values comparable to those in other research studies, with UTS and YS ranging from 1008 ± 2 to 941 ± 9 MPa and from 682 ± 11 to 640 ± 7 MPa, respectively.

This study demonstrated that a combination of lower P values and smaller hatch spacings can effectively strengthen Ni625 alloys. It was also found that there several parameters can be set to achieve similar outcomes. Indeed, these findings pave the way for the formulation of various “recipes” in the future tailored to the shape and complexity of different parts, thus opening new avenues for part development.

Acknowledgment. The experimental assistance and invaluable discussions with Takashi Sugizaki (Nikon Corp. Advanced Technology Research & Development Materials & Advanced Research Laboratory) and Daizo Saito (Hikari Glass Co.,Ltd.) are highly appreciated.

References

[1] P. R. Gradl, T. Teasley, C. Protz, C. Katsarelis, and P. Chen, “Process Development and Hot-fire Testing of Additively Manufactured NASA HR-1 for Liquid Rocket Engine Applications,” in *Proc. 2021 AIAA Propuls. Energy Forum*, Aug. 2021.

[2] P. R. Gradl, C. Protz, and T. Wammen, “Additive manufacturing development and hot-fire testing of liquid rocket channel wall nozzles using blown powder directed energy deposition inconel 625 and jbk-75 alloys,” in *Proc. 2019 AIAA Propuls. Energy Forum Expo.*, Aug. 2019.

[3] Y. Ekubaru *et al.*, “Excellent strength-ductility balance of Sc-Zr-modified Al-Mg alloy by tuning bimodal microstructure via hatch spacing in laser powder bed fusion,” *Mater. Des.*, vol. 221, 110976, 2022.

[4] D. Svetlizky *et al.*, “Directed energy deposition (DED) additive manufacturing: Physical characteristics, defects, challenges and applications,” *Mater. Today*, vol. 49, pp. 271–295, 2021.

[5] D. Svetlizky *et al.*, “Laser-based directed energy deposition (DED-LB) of advanced materials,” *Mater. Sci. Eng. A*, vol. 840, 142967, 2022.

[6] A. Bandyopadhyay, K. D. Traxel, M. Lang, M. Juhasz, N. Eliaz, and S. Bose, “Alloy design via additive manufacturing: Advantages, challenges, applications and perspectives,” *Mater. Today*, vol. 52, pp. 207–224, 2022.

[7] J. Wang, Y. Wang, Y. Su, and J. Shi, “Evaluation of in-situ alloyed Inconel 625 from elemental powders by laser directed energy deposition,” *Mater. Sci. Eng. A*, vol. 830, 142296, 2022.

[8] T. Ünal-Saewe, L. Gahn, J. Kittel, A. Gasser, and J. H. Schleifenbaum, “Process development for tip repair of complex shaped turbine blades with IN718,” *Procedia Manuf.*, vol. 47, pp. 1050–1057, 2020.

[9] J. M. Wilson, C. Piya, Y. C. Shin, F. Zhao, and K. Ramani, “Remanufacturing of turbine blades by laser direct deposition with its energy and environmental impact analysis,” *J. Clean. Prod.*, vol. 80, pp. 170–178, 2014.

[10] V. K. Balla, S. Banerjee, S. Bose, and A. Bandyopadhyay, “Direct laser processing of a tantalum coating on titanium for bone replacement structures,” *Acta Biomater.*, vol. 6, no. 6, pp. 2329–2334, 2010.

[11] P. R. Gradl and C. S. Protz, “Technology advancements for channel wall nozzle manufacturing in liquid rocket engines,” *Acta Astronaut.*, vol. 174, pp. 148–158, 2020.

[12] S. P. Kumar, S. Elangovan, R. Mohanraj, and J. R. Ramakrishna, “A review on properties of Inconel 625 and Inconel 718 fabricated using direct energy deposition,” *Mater. Today Proc.*, vol. 46, pp. 7892–7906, 2021.

[13] A. Poudel, P. R. Gradl, S. Shao, and N. Shamsaei, “Tensile deformation behavior of laser powder direct energy deposited Inconel 625: Cryogenic to elevated temperatures,” *Mater. Sci. Eng. A*, vol. 889, 145826, 2024.

[14] J. Nguejio, F. Szmytka, S. Hallais, A. Tanguy, S. Nardone, and M. G. Martinez, “Comparison of microstructure features and mechanical properties for additive manufactured and wrought nickel alloys 625,” *Mater. Sci. Eng. A*, vol.

764, 138214, 2019.

[15] M. Rombouts, G. Maes, M. Mertens, and W. Hendrix, "Laser metal deposition of Inconel 625: Microstructure and mechanical properties," *J. Laser Appl.*, vol. 24, no. 5, 052007, 2012.

[16] Y. L. Hu, Y. L. Li, S. Y. Zhang, X. Lin, Z. H. Wang, and W. D. Huang, "Effect of solution temperature on static recrystallization and ductility of Inconel 625 superalloy fabricated by directed energy deposition," *Mater. Sci. Eng. A*, vol. 772, 138711, 2020.

[17] G. Marchese *et al.*, "Characterization and Comparison of Inconel 625 Processed by Selective Laser Melting and Laser Metal Deposition," *Adv. Eng. Mater.*, vol. 19, no. 3, 1600635, 2017.

[18] Y. L. Hu, X. Lin, X. B. Yu, J. J. Xu, M. Lei, and W. D. Huang, "Effect of Ti addition on cracking and microhardness of Inconel 625 during the laser solid forming processing," *J. Alloys Compd.*, vol. 711, pp. 267–277, 2017.

[19] Y. L. Hu *et al.*, "Effect of solution heat treatment on the microstructure and mechanical properties of Inconel 625 superalloy fabricated by laser solid forming," *J. Alloys Compd.*, vol. 767, pp. 330–344, 2018.

[20] R. Savinov, Y. Wang, and J. Shi, "Evaluation of microstructure, mechanical properties, and corrosion resistance for Ti-doped inconel 625 alloy produced by laser directed energy deposition," *Mater. Sci. Eng. A*, vol. 884, 145542, 2023.

[21] N. K. Adomako, N. Haghdadi, and S. Primig, "Electron and laser-based additive manufacturing of Ni-based superalloys: A review of heterogeneities in microstructure and mechanical properties," *Mater. Des.*, vol. 223, 111245, 2022.

[22] G. P. Dinda, A. K. Dasgupta, and J. Mazumder, "Laser aided direct metal deposition of Inconel 625 superalloy: Microstructural evolution and thermal stability," *Mater. Sci. Eng. A*, vol. 509, no. 1–2, pp. 98–104, 2009.

[23] Z. Tian *et al.*, "A review on laser powder bed fusion of inconel 625 nickel-based alloy," *Appl. Sci.*, vol. 10, no. 1, 81, 2020.

[24] D. K. Gorai and T. K. Kundu, "Density Functional Theory Study of Structural and Electronic Properties of γ'-Ni3Al and γ-Ni3Nb," *IOP Conf. Ser. Mater. Sci. Eng.*, vol. 338, no. 1, 012041, 2018.

[25] J. M. V. Quaresma, A. Carlos, and A. Garcia, "Correlation between unsteady-state solidification conditions, dendrite spacings, and mechanical properties of AI-Cu alloys," *Metall. Mater. Trans. A Phys. Metall. Mater. Sci.*, vol. 31, no. 12, pp. 3167–3178, 2000.

[26] K. S. Cruz, E. S. Meza, F. A. P. Fernandes, J. M. V. Quaresma, L. C. Casteletti, and A. Garcia, "Dendritic arm spacing affecting mechanical properties and wear behavior of Al-Sn and Al-Si alloys directionally solidified under unsteady-state conditions," *Metall. Mater. Trans. A Phys. Metall. Mater. Sci.*, vol. 41, no. 4, pp. 972–984, 2010.

[27] J. Shao, G. Yu, X. He, S. Li, R. Chen, and Y. Zhao, "Grain size evolution under different cooling rate in laser additive manufacturing of superalloy," *Opt. Laser Technol.*, vol. 119, 105662, 2019.

[28] Y. Chen, Y. Yan, and B. Li, "Thermal Analyses of Power Electronics Integrated with Vapour Chamber Cooling," *Automot. Innov.*, vol. 3, no. 4, pp. 328–335, 2020.

[29] B. K. A. Kumar, M. G. Ananthaprasad, and K. Gopalakrishna, "Action of Cryogenic chill on Mechanical properties of Nickel alloy Metal Matrix Composites," *IOP Conf. Ser. Mater. Sci. Eng.*, vol. 149, no. 1, 012116, 2016.

[30] O. Gokcekaya *et al.*, "Effect of scan length on densification and crystallographic texture formation of pure chromium fabricated by laser powder bed fusion," *Crystals*, vol. 11, no. 1, pp. 1–14, 2021.

[31] Y. Ekubaru, O. Gokcekaya, and T. Nakano, "Effects of Scanning Strategy on the Microstructure and Mechanical Properties of Sc-Zr-Modified Al-Mg Alloy Manufactured by Laser Powder Bed Fusion," *Crystals*, vol. 12, no. 10, 1348, 2022.

[32] T. DebRoy *et al.*, "Additive manufacturing of metallic components-Process, structure and properties," *Prog. Mater. Sci.*, vol. 92, pp. 112–224, 2018.

[33] W. Zhao *et al.*, "The columnar to equiaxed transition of CoCrNi medium-entropy alloy fabricated by laser directed energy deposition," *Mater. Des.*, vol. 237, 112538, 2024.

[34] Z. Zhou, L. Huang, Y. Shang, Y. Li, L. Jiang, and Q. Lei, "Causes analysis on cracks in nickel-based single crystal superalloy fabricated by laser powder deposition additive manufacturing," *Mater. Des.*, vol. 160, pp. 1238–1249, 2018.

[35] Z. Tong *et al.*, "Laser additive manufacturing of FeCrCoMnNi high-entropy alloy: Effect of heat treatment on microstructure, residual stress and mechanical property," *J. Alloys Compd.*, vol. 785, pp. 1144–1159, 2019.

[36] O. Gokcekaya, T. Ishimoto, S. Hibino, J. Yasutomi, T. Narushima, and T. Nakano, "Unique crystallographic texture formation in Inconel 718 by laser powder bed fusion and its effect on mechanical anisotropy," *Acta Mater.*, vol. 212, 116876, 2021.

[37] S. H. Sun, K. Hagihara, T. Ishimoto, R. Suganuma, Y. F. Xue, and T. Nakano, "Comparison of microstructure, crystallographic texture, and mechanical properties in Ti-15Mo-5Zr-3Al alloys fabricated via electron and laser beam powder bed fusion technologies," *Addit. Manuf.*, vol. 47, 102329, 2021.

[38] Y. L. Hu *et al.*, "Plastic deformation behavior and dynamic recrystallization of Inconel 625 superalloy fabricated by directed energy deposition," *Mater. Des.*, vol. 186, 108359,

2020.

[39] R. J. Vikram, A. Singh, and S. Suwas, "Effect of heat treatment on the modification of microstructure of selective laser melted (SLM) IN718 and its consequences on mechanical behavior," *J. Mater. Res.*, vol. 35, no. 15, pp. 1949–1962, 2020.

[40] J. N. Zhu, E. Borisov, X. Liang, E. Farber, M. J. M. Hermans, and V. A. Popovich, "Predictive analytical modelling and experimental validation of processing maps in additive manufacturing of nitinol alloys," *Addit. Manuf.*, vol. 38, 101802, 2021.

[41] M. S. Pham, B. Dovgyy, P. A. Hooper, C. M. Gourlay, and A. Piglione, "The role of side-branching in microstructure development in laser powder-bed fusion," *Nat. Commun.*, vol. 11, no. 1, 749, 2020.

[42] Z. Gan, G. Yu, X. He, and S. Li, "Numerical simulation of thermal behavior and multicomponent mass transfer in direct laser deposition of Co-base alloy on steel," *Int. J. Heat Mass Transf.*, vol. 104, pp. 28–38, 2017.

[43] L. E. dos Santos Paes, M. Pereira, F. A. Xavier, W. L. Weingaertner, and L. O. Vilarinho, "Lack of fusion mitigation in directed energy deposition with laser (DED-L) additive manufacturing through laser remelting," *J. Manuf. Process.*, vol. 73, pp. 67–77, 2022.

恵久春佑寿夫　Yusufu EKUBARU
アドバンストマニュファクチャリング事業部 第二開発部
2nd Development Department
Advanced Manufacturing Business Unit

中林拓頌　Takuya NAKABAYASHI
先進技術開発本部 数理技術研究所
Mathematical Sciences Research Laboratory
Advanced Technology Research ＆ Development

藤原朋春　Tomoharu FUJIWARA
アドバンストマニュファクチャリング事業部 第二開発部
2nd Development Department
Advanced Manufacturing Business Unit

Behrang POORGANJI
Morf3D Inc.